Time-resolving tunneling ionization via strong-field photoelectron holography

Jia Tan,[1] Yueming Zhou,[1,*] Mingrui He,[1] Qinghua Ke,[1] Jintai Liang,[1] Yang Li,[1] Min Li,[1] and Peixiang Lu[1,2,†]

[1]*School of Physics, Huazhong University of Science and Technology, Wuhan 430074, China*

[2]*Hubei Key Laboratory of Optical Information and Pattern Recognition, Wuhan Institute of Technology, Wuhan 430205, China*

(Received 26 December 2018; published 4 March 2019)

Strong-field tunneling ionization is the initial step for various ultrafast dynamics in intense laser-atom and/or molecule interactions. Time-resolving tunneling ionization is of crucial importance for accurately understanding these ultrafast processes. In our previous work [Phys. Rev. Lett. **121**, 253203 (2018).], we proposed an attosecond photoelectron interferometer based on strong-field photoelectron holography to resolve the tunneling ionization. Here, we show more details about how the complex ionization time of tunneling is retrieved with our scheme. We demonstrate that the Coulomb interaction, which is a tedious and complex problem in dealing with photoelectron interference in strong-field ionization, can be safely canceled in our scheme. This is further confirmed by performing our scheme for both the model atoms with short-range and Coulomb potentials. Additionally, the validity and accuracy of our scheme are confirmed by its application in different targets and different laser parameters. Our scheme provides a reliable and versatile method to resolve the time information of strong-field tunneling ionization.

DOI: 10.1103/PhysRevA.99.033402

I. INTRODUCTION

Laser-induced tunneling ionization of atoms and molecules is one of the most fundamental strong-field processes and it serves as the first step for plenty of processes in attosecond science [1–4]. When an atom or a molecule is exposed to an intense laser pulse, the bound electron can be tunneling ionized through the potential barrier. The ionized electron wave packet (EWP) is further accelerated by the oscillating electric field of the laser pulse. Part of the EWP could be driven back to scatter off or recombine with the atomic or molecular core, producing various nonlinear phenomena [5] such as above-threshold ionization [6–8], nonsequential double ionization [9–15], and high-order harmonic generation [16–20]. In past decades, these phenomena have been widely applied to the attosecond community, including attosecond pulse generation [21–24], molecular tomography [25,26], and laser-induced electron diffraction [27–30]. In these ultrafast processes and their applications, one of the most important questions concerns the temporal properties of the tunneling ionization, i.e., the time when the process is initiated.

In the past ten years, this question has draw much attention and has been hotly discussed [31]. Recently, rapidly developing attosecond technology has facilitated measurement with unprecedented temporal resolution, which opens up the opportunity to revisit this fundamentally important question [32–36]. For example, by applying the attoclock technique, the tunneling time of the electron has been experimentally measured with attosecond resolution [32]. The measured results indicate that the tunneling time is negligibly small. In the attoclock technique, the tunneling time is defined as the time delay between the maximum of the electric field and the maximal probability of electron emission. Quantum mechanically, the electron is described by wave function. In the presence of the laser field, the electron wave function continuously extends from the inner barrier to the outer barrier [37]. The different ionization instants correspond to the different measured momenta of electrons and the orders of the resultant harmonics.

In recent years, many experimental and theoretical efforts have been made to determine the ionization time related to the observables. For example, through high-order harmonic spectroscopy, the ionization time for each harmonic order in high-harmonic generation was reconstructed [38,39]. The reconstructed results agree well with the predictions of the quantum-orbit (QO) model [7]. The QO model physically originates from the application of Feynman's path-integral approach in strong-field laser-atom interaction. In the QO model, the ionization time is complex. Its real part denotes the time when the electron exits the tunneling barrier. The imaginary part is interpreted as the tunneling time that characterizes the under-barrier electron motion [7,40,41]. This concept was first proposed in the pioneering paper of the strong-field physics by Keldysh and later was further developed and demonstrated by a wide range of theoretical literature [42–45]. During past years, it has been reported that the complex ionization time is crucially important for revealing the attosecond dynamics of the strong-field ionization process in time-resolving experiments [46–51]. It is also vital for exploring the nonadiabatic effect in the tunneling process, which has been of great concern [52–56]. Therefore, accurately retrieving this time is essential for fully understanding the strong-field processes and for further performing their applications. In Ref. [38], the real part of the ionization time is reconstructed. In Ref. [39], the imaginary part of the ionization time is reconstructed based on some assumptions about the real part

*Corresponding author: zhouymhust@hust.edu.cn

†Corresponding author: lupeixiang@hust.edu.cn

of the ionization time and the rescattering time. Actually, it has been pointed out that these assumptions significantly affect the accuracy of the time retrieval [57].

Complementary to the measurements based on harmonic spectra, strong-field photoelectron holography (SFPH) is expected to be a powerful tool to probe the ultrafast electron dynamics in tunneling ionization. The SFPH interference derives from the interference of the near-forward rescattering EWP (which recollides with the parent ion after tunneling ionization) and the direct EWP (which drifts to the detector directly after tunneling ionization). This interference has been identified in a recent experiment with xenon [58] and then observed for other atoms [59–62] and molecules [63,64], and has been widely analyzed [65–75]. It was pointed out that the SFPH interference has the potential for probing the structural and temporal properties of atomic and molecular systems with angstrom and attosecond precision [58]. To date, this SFPH has been applied to experimentally reveal the tunneling exit point in atomic tunneling ionization [59]. The initial phase of tunneling EWP has been extracted from the SFPH pattern [63,69]. Recently, we have theoretically demonstrated that with SFPH the phase of the scattering amplitude of the atoms and molecules can be extracted [71]. More interestingly, we have shown that the charge migration in molecules can be directly visualized by analyzing the SFPH structure [75].

Very recently, we proposed that with SFPH both the ionization and rescattering times of the electron in the tunneling ionization can be accurately determined [76]. The method is closely analogous to the optical Michelson interferometer. In the traditional Michelson interferometer, a light source is split into two arms, each of which is reflected back toward the light beam-splitter mirror, as shown in Fig. 1(a). The amplitudes of these arms are combined through the superposition principle on the screen, resulting in an interferogram. By analyzing the interferogram fringes, the path characterizing the two arms could be inferred. In our scheme, the tunneling ionized EWP plays as the source of the Michelson interferometer, and the direct and near-forward rescattering EWPs act as its two arms, as shown in Fig. 1(b). Due to the coherent nature of EWPs, these two kinds of EWP can induce the SFPH pattern in the photoelectron momentum distribution (PEMD) [58]. When an orthogonally polarized perturbative pulse is added to the fundamental (FM) driving field, the paths of these two EWPs are modified and thus a displacement of the interference fringes is manifested in the PEMDs. Analyzing the response of the interference fringes to the perturbation enables us to retrieve the time information of the paths of the EWPs. This introduces us to the attosecond photoelectron interferometer.

In this paper, we follow our previous work [76] and show more details about how the complex ionization time and the associated rescattering time for strong-field tunneling ionization are retrieved. In our work, the PEMDs are calculated by solving the time-dependent Schrödinger equation, from which the SFPH structure is extracted. Note that in intense laser-atom and/or molecule interactions, the influence of the Coulomb interaction is a very tough problem and it impedes the information extraction from the PEMDs. Moreover, it has been demonstrated that the Coulomb potential significantly affects the spacing of the SFPH fringes and induces unexpected structure [65,77–83]. Therefore, dealing with the

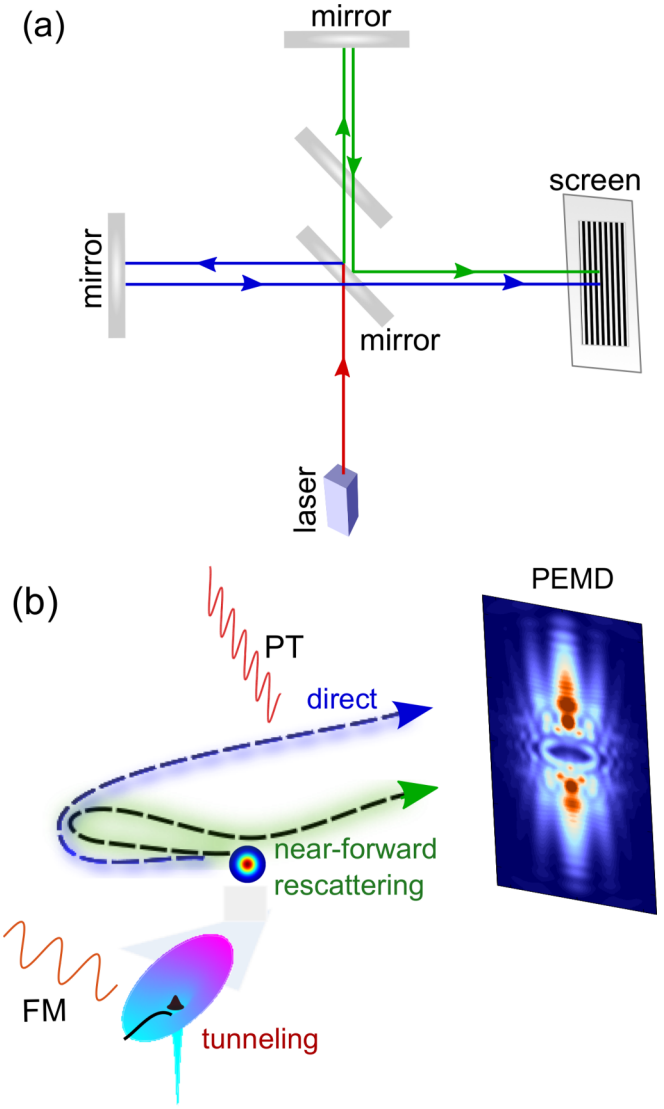

FIG. 1. (a) The schematic diagram of the Michelson interferometer. The red line indicates the light source. The blue and green lines represent the two arms of the interferometry. The light waves propagating along these two arms are superimposed coherently on the screen, producing the interferogram. (b) Our attosecond photoelectron interferometer. Strong-field tunneling ionization of the atom and/or molecule produces an electron wave packet (EWP). This EWP reaches the detector through two paths. In one path, the EWP reaches the detector directly (direct electron) and in the other path the EWP undergoes a near-forward rescattering with the parent ion (rescattering electron) before reaching the detector, giving rise to the interference structure in the photoelectron momentum distribution (PEMD). When an orthogonally polarized laser field as a perturbation (PT) is introduced, both paths are disturbed, resulting in the shift of the holographic interference fringes.

SFPH interference in strong-field ionization could be tedious and complex. In our scheme, we demonstrate that the complex influence of the Coulomb correlation on the response of the SFPH fringes to the orthogonal perturbation can be safely canceled and thus the time retrieval processes are greatly simplified. We further show that our scheme works well for both the model atoms with the Coulomb and short-range

potentials. Our retrieved results exhibit excellent agreement with the predictions of the QO model. In addition, we confirm the validity and accuracy of our scheme by applying it to different atomic systems and different laser parameters. Our work provides a reliable and versatile way to measure the temporal properties of strong-field tunneling ionization.

II. THEORETICAL METHODS

In our scheme, the orthogonal two-color (OTC) field combined by a strong fundamental field and an orthogonally polarized perturbative field is used. The strong FM field induces the ionization of atoms. The orthogonal perturbation, which is much weaker than the FM field, does not affect the ionization of the electron, while it can affect the phase of the electron during the propagation. This is essential in the attosecond photoelectron interferometer. The electric field $\vec{E}(t)$ of this OTC pulse is written as

$$\vec{E}(t) = f(t)[E_x \cos(\omega t)\vec{x} + E_y \cos(q\omega t + \varphi)\vec{y}], \tag{1}$$

where the FM component of the electric field $\vec{E}(t)$ is polarized along the x axis and the orthogonal component is polarized along the y axis (perpendicular to the x axis). E_x and E_y are the amplitudes of the FM and the orthogonal components, respectively. ω is the angular frequency of the FM component. $q\omega$ represents the angular frequency of the orthogonal component, which is tunable. φ is the relative phase of the OTC field. $f(t)$ is the envelope function of the electric field, which has the trapezoidal form, ramping on and off over one optical cycle with a plateau of three periods of the FM pulse.

A. Numerically solving TDSE

With the above OTC field, we investigate the ionization of atoms by solving the two-dimensional time-dependent Schrödinger equation (TDSE) with the single-active-electron approximation. The TDSE reads [atomic units (a.u.) are used throughout unless otherwise stated]

$$i\frac{\partial \Psi(\vec{r},t)}{\partial t} = H(\vec{r},t)\Psi(\vec{r},t), \tag{2}$$

where $\Psi(\vec{r},t)$ represents the wave function and $\vec{r} = (x,y)$ denotes the electron position in the polarization plane of the OTC field. In length gauge, the Hamiltonian $H(\vec{r},t)$ is written as

$$H(\vec{r},t) = -\frac{1}{2}\nabla^2 + V(r) + \vec{r}\cdot\vec{E}(t), \tag{3}$$

where $V(r) = -1/\sqrt{x^2+y^2+a}$. a is the soft-core parameter, which is selected to match the ground-state energy of atom. For xenon ($I_p = 0.446$ a.u.), a is set to be 0.92, and for argon ($I_p = 0.581$ a.u.), a is set as 0.39.

To numerically solve the TDSE, the split-operator spectral method on a Cartesian grid is employed [84]. The initial wave function is prepared by imaginary-time propagation [85]. It is further smoothly split into two parts: the inner $(0 - R_s)$ and outer $(R_s - R_{max})$ regions in real-time propagation. At any given time τ, the electron wave function $\Psi(\tau)$ is given by [86]

$$\begin{aligned}\Psi(\tau) &= \Psi(\tau)[1 - F_s(R_s)] + \Psi(\tau)F_s(R_s)\\ &= \Psi_I(\tau) + \Psi_O(\tau).\end{aligned} \tag{4}$$

Here $F_s(R_s) = 1/[1 + e^{-(r-R_s)/\Delta}]$ is the splitting function. Δ represents the width of the crossover region and R_s is the boundary of the inner space [87]. In the inner space, the wave function $\Psi_I(\tau)$ is propagated under full Hamiltonian, while in the outer space, the wave function $\Psi_O(\tau)$ stands for the "ionized part" analytically propagating under the Volkov Hamiltonian [86,88]. Specially, at each time step τ, the ionized EWP in the outer space is firstly transformed into momentum space $C(\vec{p},\tau)$ and then it is propagated from time τ to the end of the laser pulse. Finally, we obtain the PEMD related to the sum of the wave function in momentum space at τ,

$$\frac{dP(\vec{p})}{dEd\theta} = \sqrt{2E}\left|\sum_{\tau}\overline{C}(\vec{p},\tau)\right|^2, \tag{5}$$

where $\overline{C}(\vec{p},\tau) = e^{-i\int_{\tau}^{\infty}\frac{1}{2}[\vec{p}+\vec{A}(\tau')]^2 d\tau'}C(\vec{p},\tau)$. $E = \vec{p}^2/2$ represents the electron final energy and θ is the angle between the electron final momentum $\vec{p}$ and the polarization direction of the FM field. $\vec{A}(\tau) = -\int_{-\infty}^{\tau}\vec{E}(t)dt$ is the vector potential of the OTC field.

In our simulation, the Cartesian grid ranges from –700 to 700 a.u. for both x and y directions with a grid size of $\Delta x = \Delta y = 0.34$ a.u. The boundary of the inner space R_s is set to be 200 a.u. with the width of crossover region $\Delta = 8$ a.u. The propagation time step of the wave function δt is equal to 0.05 a.u. At the end of the pulse, the wave function is propagated for three additional optical cycles of the FM field to make sure the "slow" electrons reach the boundary R_s [67,89].

B. Quantum-orbit model

Our interferometer is based on the SFPH. The SFPH structure of the PEMD derives from the interference of the direct and near-forward rescattering EWPs, and it is given by

$$\begin{aligned}M^2(\vec{p}) &= |M_d(\vec{p}) + M_r(\vec{p})|^2\\ &= |M_d(\vec{p})|^2 + |M_r(\vec{p})|^2 + 2|M_d(\vec{p})||M_r(\vec{p})|\cos(\delta\theta).\end{aligned} \tag{6}$$

$M_d(\vec{p})$ and $M_r(\vec{p})$ represent the ionization amplitudes of the direct and rescattering EWPs, respectively. $\delta\theta$ is the phase difference between these two categories of EWP, which has the form [71]

$$\delta\theta = \delta\theta_F + \alpha, \tag{7}$$

where α represents the phase for the interaction of the rescattering electron with the target ion, and $\delta\theta_F$ accounts for the phase difference between the direct and rescattering EWPs accumulated during their propagation in the laser field.

Following Ref. [58], the phase $\delta\theta_F$ can be calculated with the saddle-point approximation, which provides us the

quantum orbit to analyze the SFPH interference [90]. In the OTC field, $\delta\theta_F$ is written as

$$\begin{aligned}\delta\theta_F = &\frac{1}{2}\int_{t_i^D}^{t_r}[p_y + A_y(t)]^2 dt + \frac{1}{2}\int_{t_i^D}^{t_r}[p_x + A_x(t)]^2 dt \\ &- \frac{1}{2}\int_{t_i^R}^{t_r}[k_y + A_y(t)]^2 dt - \frac{1}{2}\int_{t_i^R}^{t_r}[k_x + A_x(t)]^2 dt \\ &+ I_p(t_i^R - t_i^D),\end{aligned} \tag{8}$$

where $A_x(t)$ and $A_y(t)$ indicate the vector potential of the FM and orthogonal components of the OTC field, respectively. p_x and p_y are the final parallel momentum (along the x axis) and transverse momentum (along the y axis) of the electron. k_x and k_y denote the parallel and transverse components of the canonical momentum $\vec{k}$ of the electron before rescattering. I_p is the ionization potential of the atom. t_i^D is the ionization time of the direct electron. t_i^R and t_r are the ionization and rescattering times of the rescattering electron. At the given time t, the momenta of the rescattering electron along the polarization directions of the FM field and the orthogonal perturbation before rescattering are $k_x + A_x(t)$ and $k_y + A_y(t)$, while those of the direct electron are $p_x + A_x(t)$ and $p_y + A_y(t)$.

In our study, the orthogonal component of the OTC field is very weak, and thus the ionization and rescattering times can be approximately determined by the saddle-point equation in the FM field. For the direct electron, the saddle-point equation is written as

$$\frac{1}{2}[p_x + A_x(t_i^D)]^2 + \frac{1}{2}p_y^2 + I_p = 0, \tag{9}$$

while for the rescattering electron, it reads

$$\begin{aligned}&\frac{1}{2}[k_x + A_x(t_i^R)]^2 + I_p = 0, \\ &\frac{1}{2}[k_x + A_x(t_r)]^2 = \frac{1}{2}[p_x + A_x(t_r)]^2 + \frac{1}{2}p_y^2, \\ &\int_{t_i^R}^{t_r}[k_x + A_x(t)]dt = 0, \\ &\int_{t_i^R}^{t_r}[k_y + A_y(t)]dt = 0.\end{aligned} \tag{10}$$

Here Eq. (9) stands for the energy conservation for the direct electron at tunneling ionization. The first and second equations in Eq. (10) indicate the energy conservation for the rescattering electron during tunneling ionization and rescattering, respectively. The third and fourth equations in Eq. (10) represent the return conditions.

It should be noted that with the QO method, the obtained ionization and rescattering times are complex numbers, so all the quantities except the measured final momenta p_x and p_y are complex numbers, and thus $\delta\theta$ in Eq. (7) is also complex. In our scheme, the imaginary part of the phase $\delta\theta$ affects the amplitudes of the direct and rescattering electrons and influences the visibility of the interference fringes. It is the real part of $\delta\theta$ determines the position of the interference fringes that we focus on. Therefore in this paper, we consider only the real part of $\delta\theta$.

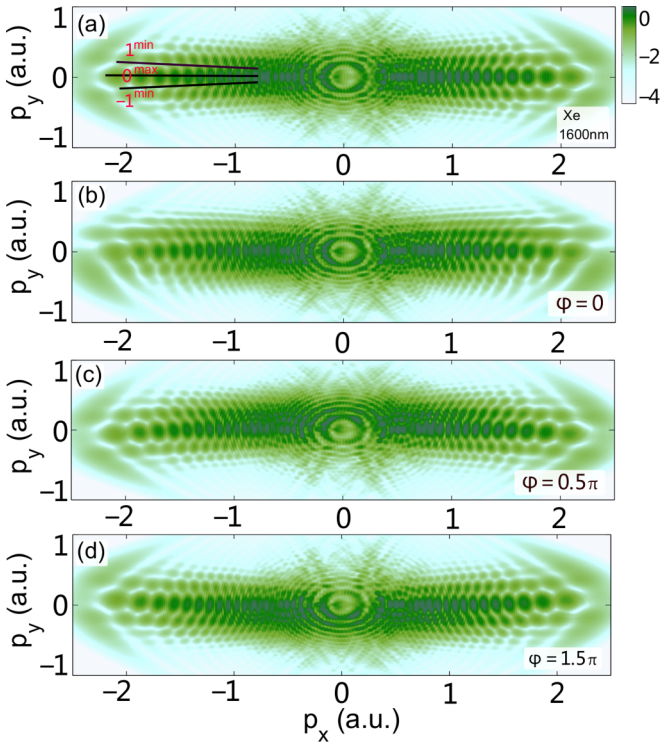

FIG. 2. (a) PEMD for strong-field tunneling ionization of a xenon atom by a 1600-nm single-color laser field in the log scale. The black lines indicate the positions of SFPH interference fringes (from top to bottom: the first-order minimum labeled by 1^{min} at $p_y > 0$, the zeroth-order maximum labeled by 0^{max}, and the minus first-order minimum labeled by -1^{min} at $p_y < 0$). (b)–(d) PEMDs for the OTC field combined by a strong 1600-nm FM field and a weak second harmonic with relative phase $\varphi = 0$, 0.5π, 1.5π, respectively. The intensity of the 1600-nm laser field is 1.5×10^{14} W/cm^2 and of the 800-nm pulse 1.0×10^{12} W/cm^2.

III. RESULTS AND DISCUSSION

A. Photoelectron momentum distributions obtained by solving TDSE

In Fig. 2, we show the photoelectron momentum distributions (PEMDs) for strong-field tunneling ionization of xenon atoms obtained by solving the TDSE. Figure 2(a) shows the result in the 1600-nm single-color field only. Figures 2(b)–2(d) display the results in the OTC field consisting of a strong 1600-nm FM field polarized along the x axis and a weak 800-nm pulse polarized along the y axis with relative phase $\varphi = 0$, 0.5π and 1.5π, respectively. The intensity of the 1600-nm laser field is 1.5×10^{14} W/cm^2, and that of the second harmonic is 1.0×10^{12} W/cm^2. In these PEMDs, there are three types of prominent interference fringes. The ringlike structure centered around zero momentum is the intercycle interference, known as the ATI peaks. The nearly vertical fringes, most visible on the p_x axis, come from the interference of the direct electrons tunneling ionized during two adjacent half cycles of the laser pulse [91–93]. Due to the

laser focal volume effect, these two types of interference are usually invisible in experiments. The other nearly horizontal fringes marked by the black lines in Fig. 2(a) are referred to as the SFPH pattern, which originates from the interference of the electrons reaching the detector directly after tunneling and those near-forward rescattering with the target ion [71]. This SFPH pattern has been observed in a broad range of experiments and is the most pronounced interference structure in the PEMDs for the near- and mid-infrared laser pulses [58,94]. In the present paper, we focus on this interference pattern. For the single-color field, the holographic structure is exactly symmetric about $p_y = 0$, as displayed in Fig. 2(a), while for the OTC field, the paths of tunneling ionized electrons are disturbed by the orthogonal second harmonic, resulting in the shift of the interference fringes, as shown in Figs. 2(b)–2(d). Interestingly, depending on the parallel momentum p_x, the fringe shift is changing with relative phase φ. As we will show below, this shift and its p_x dependence provide us with information about the electron tunneling ionization.

B. Holographic fringes extracted from PEMD

To make the SFPH fringes and their shift more visible, we first wash out the vertical fringes by averaging the raw PEMD over p_x with a window function [71]. Several cuts of the obtained PEMD at different p_x are displayed in Figs. 3(a) and 3(b), where the effect of the orthogonal second harmonic of the OTC field can be clearly seen. For instance, for $p_x = -1.1$ a.u., the interference minima shift towards right and left in the OTC field at $\varphi = 0$ and $\varphi = \pi$ with respect to the single-color field, respectively. For $p_x = -1.6$ a.u., the shift is reversed. Then we utilize the procedure introduced in [71] to eliminate the envelop of the PEMD induced by the ionization amplitude of the electrons and extract the interference term $\cos(\delta\theta)$ between the direct and rescattering electrons. Figures 3(c) and 3(d) separately display the examples of the obtained interference term $\cos(\delta\theta)$ in the single-color field and the OTC field with $\varphi = 0.5\pi$ as functions of transverse momentum p_y for p_x ranging from –2 to 2 a.u. One can see two types of interference fringes. The irregular one, visible in the momentum region $|p_x| \in [0, 0.4]$ a.u., is identified as the holographic interference which formed by the multiple forward-scattering electrons [95]. The obvious regular fringes in the momentum region $|p_x| \in [0.4, 2]$ a.u. are the SFPH structure that we are interested in here. Clearly, for the single-color field this structure is exactly symmetric about $p_x = 0$ and $p_y = 0$. For the OTC field, the positions of the interference minima and maxima of this SFPH structure are also symmetric with respect to $p_x = 0$, while for $p_y = 0$, it is obviously asymmetric. For a better view, we display the cut of $\cos(\delta\theta)$ at $p_x = -1.1$ a.u. for the single-color field and for the OTC field with relative phase $\varphi = 0$, π, 0.5π, and 1.5π in Fig. 3(e). We also show $\cos(\delta\theta)$ for another cut at $p_x = -1.6$ a.u. in Fig. 3(f). It is indicated that the positions of the interference maxima and minima which depend on p_x are sensitive to the relative phase φ. At last, we monitor the positions of the interference maxima and minima for the single-color field and the OTC field in the momentum region $p_x < 0$, as shown in Fig. 3(g). It is more obvious that for the OTC field the SFPH structure shifts along the p_y direction

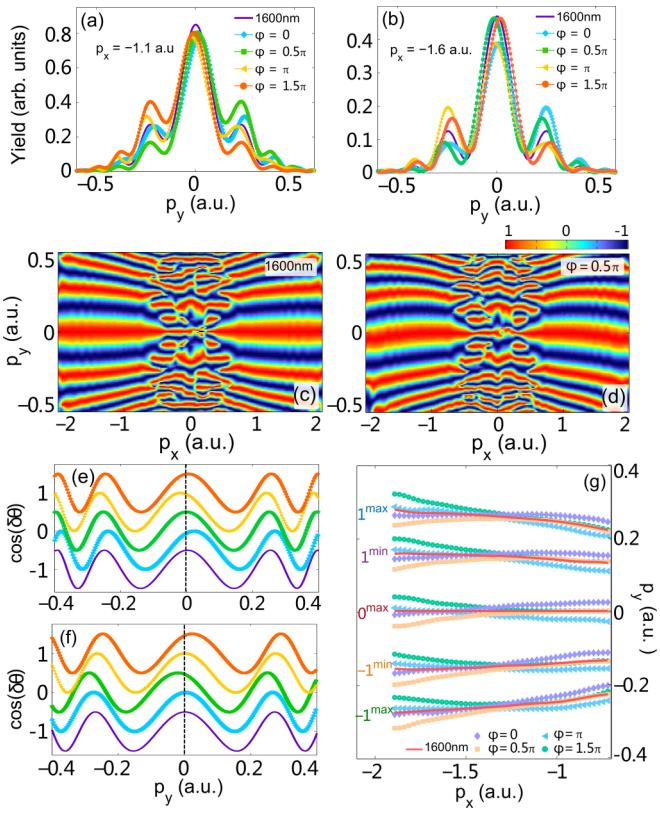

FIG. 3. (a) The PEMD obtained from the TDSE calculations at $p_x = -1.1$ a.u. for the 1600-nm single-color field (solid purple curve) and for the OTC field with relative phase $\varphi = 0$ (blue diamonds), 0.5π (green squares), π (yellow triangles), and 1.5π (red circles), respectively. (b) The same as (a) but at $p_x = -1.6$ a.u. (c) The interference term $\cos(\delta\theta)$ extracted from the PEMD in the single-color field for $p_x \in$ [-2, 2] a.u. (d) The same as (c) but for the OTC field with $\varphi = 0.5\pi$. (e) The cuts of the interference term $\cos(\delta\theta)$ at $p_x = -1.1$ a.u. in the single-color field (solid purple curve) and in the OTC field with $\varphi = 0$ (blue diamonds), 0.5π (green squares), π (yellow triangles), and 1.5π (red circles), respectively. For a better view, these curves have been shifted up and down. The dashed black line indicates the p_x axis. (f) The same as (e) but at $p_x = -1.6$ a.u. (g) The positions of the interference minima and maxima of $\cos(\delta\theta)$ as functions of p_y with respect to p_x ranging from –1.95 to –0.75 a.u. The data of red solid curves are calculated for the single-color field, and the data of diamonds, squares, triangles, and circles are obtained from the OTC field with $\varphi = 0$, 0.5π, π, and 1.5π, respectively. The five parts of the pattern from top to bottom are the first-order maxima ($1^{\max}$) and minima ($1^{\min}$) at $p_y > 0$, the zeroth-order maxima ($0^{\max}$) and the minus first-order minima ($-1^{\min}$) and maxima ($-1^{\max}$) at $p_y < 0$, respectively.

with respect to that for the single-color field, and this shift is significantly modified by relative phase.

To show the shift of the SFPH interference fringes and its p_x dependence quantitatively, we seek the position of the first interference minimum ($1^{\min}$) as a function of relative phase φ in the OTC field and calculate its shift relative to the position in the single-color field. Figure 4(a) displays the obtained result. It clearly indicates that the shift Δp_y oscillates with φ. The oscillation amplitude and the corresponding relative phase at which Δp_y maximizes vary gradually with p_x. For

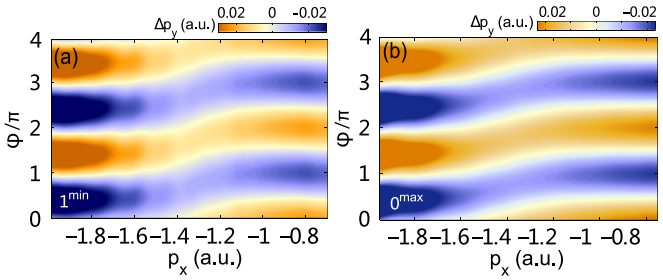

FIG. 4. (a) The position shift Δp_y of the first-order minimum of the SFPH fringes as a function of φ for p_x ranging from –1.95 to –0.75 a.u. (b) The same as (a) but monitoring the shift Δp_y for the zeroth-order maximum of the interference fringes.

example, Δp_y maximizes at $\varphi = 1.5\pi$ for $p_x = -1.8$ a.u. and maximizes at $\varphi = 2\pi$ for $p_x = -0.9$ a.u. For comparison, we also display the shift for the zeroth-order maximum ($0^{\max}$) of the interference fringes in Fig. 4(b). The obtained result is exactly the same as that for the first-order minimum of interference fringes shown in Fig. 4(a).

We can also trace the photoelectron yield at $p_y = 0$ as a function of the relative phase of the OTC field. In the single-color field, this yield maximizes at $p_y = 0$. When an orthogonal perturbation is added, the photoelectron is blown away from $p_y = 0$ by an amount of the vector potential $A_y(t_i^D, \varphi)$. Thus, the position of the maximum in the PEMD locates at $p_y = 0$ only when the vector potential $A_y(t_i^D, \varphi) = 0$. With this relation, it has been shown that the ionization time for each parallel momentum can be extracted by monitoring the photoelectron yield in the PEMD at $p_y = 0$ [96,97]. In Fig. 5(a), we display the ionization yield of photoelectron at $p_y = 0$ in the OTC field with respect to that of the single-color field, $\Delta Y = (Y^{OTC} - Y^{SC})/Y^{SC}$, where Y^{SC} and Y^{OTC} are the

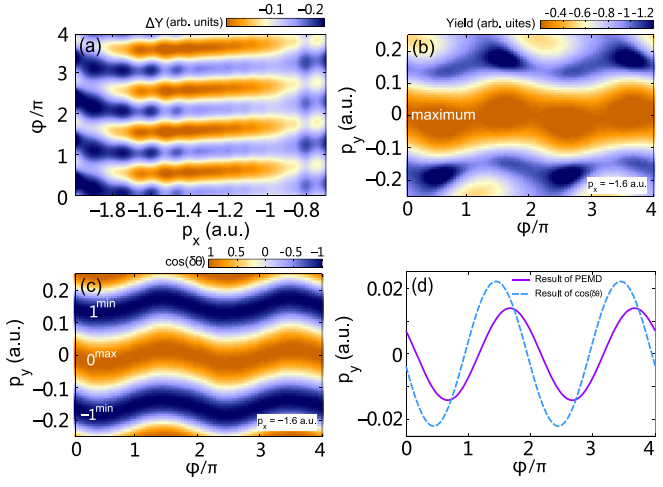

FIG. 5. (a) The relative yield $\Delta Y = (Y^{\rm OTC} - Y^{\rm SC})/Y^{\rm SC}$ at $p_y = 0$ as a function of φ for p_x ranging from –1.95 to –0.75 a.u. (b) The PEMD at $p_x = -1.6$ a.u. for different φ. (c) The same as (b) but for the interference term $\cos(\delta\theta)$. $1^{\min}$, $0^{\max}$, and $-1^{\min}$ indicate the positions of the first-order minimum, zeroth-order maximum, and the minus first-order minimum of the SFPH fringes, respectively. (d) Tracing the positions of the maximum in (b) (solid purple curve) and $0^{\max}$ in (c) (dashed blue curve) as functions of φ.

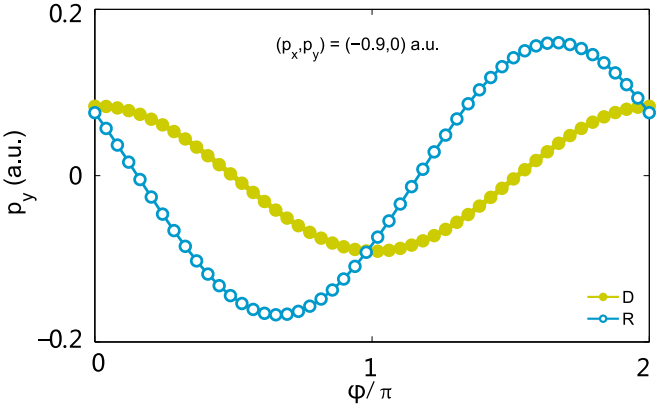

FIG. 6. The dependence of the final transverse momentum of an example photoelectron on the relative phase of the OTC field. The momentum of this example photoelectron is $(p_x, p_y) = (-0.9, 0)$ a.u. in the 1600-nm single-color field. The dots and open circles present the results for the photoelectron reaching the detector directly or undergoing a forward rescattering, respectively.

photoelectron yields in the single-color and OTC fields at $p_y = 0$, respectively. It is shown that ΔY periodically changes with φ. As the parallel momentum p_x changes, the phase φ where ΔY maximizes varies gradually. This p_x dependence of the relative phase provides us an another intuitive observation.

Note that the transverse momentum where the photoelectron yield maximizes in PEMD is not coincident with the zeroth-order maximum of the SFPH interference fringes in $\cos(\delta\theta)$. To illustrate this, in Figs. 5(b) and 5(c) we show the PEMD and $\cos(\delta\theta)$ at $p_x = -1.6$ a.u. as functions of φ, respectively. There is a phase shift between the PEMD and $\cos(\delta\theta)$. This shift is more clearly seen in Fig. 5(d), where we trace the position of the maximum in PEMD and the zeroth-order maximum in $\cos(\delta\theta)$ at $p_x = -1.6$ a.u. as functions of φ. It is shown that the maximum in PEMD shifts most away from $p_y = 0$ at $\varphi = 1.7\pi$, while it is at $\varphi = 1.4\pi$ for the interference term $\cos(\delta\theta)$. The reason is demonstrated as follows.

For the photoelectron yield at $p_y = 0$, the direct electron has the dominant contribution. Thus, the behavior of the relative yield ΔY as a function of the relative phase is a representation of the response of the direct electron to the orthogonal perturbation [96,98], while for the interference term $\cos(\delta\theta)$, it contains both contributions of the direct and rescattering electrons. Thus, the response of Δp_y to the relative phase φ is different from that of ΔY. We should mention that in the OTC field, the response of the direct electron to the relative phase φ is quite different from that of the rescattering electron. Taking the photoelectron with momentum $(p_x, p_y) = (-0.9, 0)$ a.u. in the single-color field as an example, we treat it as the direct or rescattering electron and calculate its final transverse momentum in the OTC field, as shown in Fig. 6. Obviously, the final transverse momentum for the direct electron maximizes at $\varphi = 2\pi$, while for the rescattering electron it maximizes at $\varphi = 1.7\pi$.

Summarizing, from the PEMDs we can obtain three independent observations: the amplitude of the SFPH fringes shift, and the corresponding relative phase where Δp_y peaks

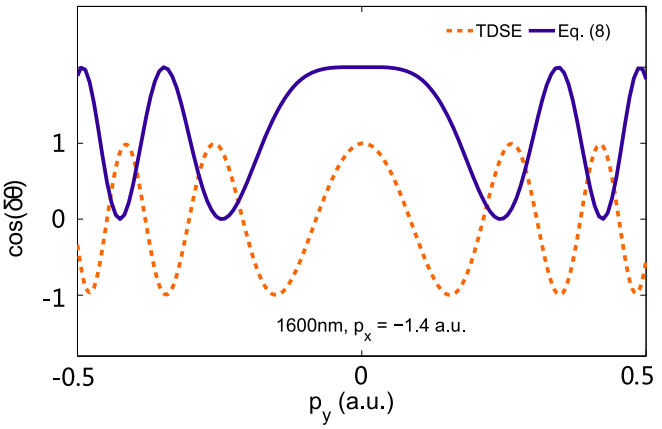

FIG. 7. The cuts of $\cos(\delta\theta)$ extracted from the TDSE results and calculated by Eq. (7), but α is not contained [i.e., Eq. (8)] for 1600-nm single-color field at $p_x = -1.4$ a.u.

[as shown in Fig. 4(a)] and the relative phase where ΔY maximizes [as indicated in Fig. 5(a)]. As explained above, the observation in ΔY reflects the disturbance of the orthogonal second harmonic on the yield of the direct electron at $p_y = 0$ [96,97]. The observations in Δp_y originate from the perturbation of the orthogonal second harmonic to the phase difference of the direct and near-forward rescattering electrons, as shown in detail in the following sections.

C. Shift of the holographic fringes and effect of the Coulomb interaction

In this section, we reveal the origin of the SFPH interference fringe shift Δp_y in the PEMDs for the OTC field with respect to the single-color field and the effect of the Coulomb interaction on this shift. It should be mentioned that in the pioneering work on the SFPH, the effects of the Coulomb interaction on the phase difference between the direct and rescattering electrons are not taken into account, and thus the predictions of the SFPH fringes deviate from the TDSE calculations and experimental data [58,65]. This point is clearly indicated in Fig. 7, where we show the interference term $\cos(\delta\theta)$ extracted from the TDSE results and calculated by the Eq. (7) but without α. In our previous work [71], we pointed out the term α, which accounts for the interaction between the parent ion and the rescattering electron (i.e., the phase of the scattering amplitude). With this term included, the SFPH pattern given by Eq. (7) agrees excellently with the TDSE result. However, the calculation about this term α is complicated and tedious, and it makes the information extraction from the photoelectron spectra very difficult. Fortunately, as addressed in the following text, this Coulomb effect does not matter for the observations of the SFPH fringe shift and can be canceled out safely.

First, we simplify the formula of the phase difference $\delta\theta_F$ given in Eqs. (7) and (8). For the near-forward rescattering SFPH, the interference fringes exist at small p_y, and thus we have $p_x \doteq k_x$ through the second equation of Eq. (10). Then it can be easily proved that the second, fourth, and fifth terms in

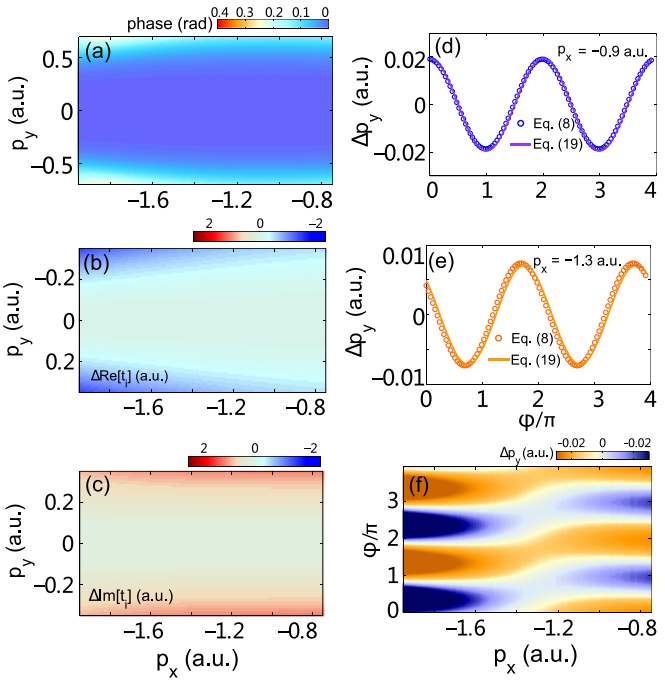

FIG. 8. (a) The value of $\frac{1}{2}\int_{t_i^D}^{t_r}(p_x+A_x)^2dt - \frac{1}{2}\int_{t_i^R}^{t_r}(k_x+A_x)^2dt + I_p(t_i^R - t_i^D)$ in Eq. (8). (b) The difference between the real parts of the ionization times for the direct and near-forward rescattering electrons. (c) The same as (b) but for the difference of the imaginary parts. (d) The shifts Δp_y of the first-order minimum of the SFPH interference fringes obtained by Eq. (8) (open circles) and calculated by Eq. (19) (solid curve) as functions of φ at $p_x = -0.9$ a.u. (e) The same as (d) but for the cut at $p_x = -1.3$ a.u. (f) Δp_y calculated by Eq. (19) as a function of φ for p_x ranging from –1.95 a.u. to –0.75 a.u.

the right side of Eq. (8) can be approximately canceled by

$$\begin{aligned}
&\frac{1}{2}\int_{t_i^D}^{t_r}(p_x+A_x)^2dt - \frac{1}{2}\int_{t_i^R}^{t_r}(k_x+A_x)^2dt + I_p\left(t_i^R - t_i^D\right)\\
&\doteq \frac{1}{2}\int_{t_i^D}^{t_r}(k_x+A_x)^2dt - \frac{1}{2}\int_{t_i^R}^{t_r}(k_x+A_x)^2dt + I_p\left(t_i^R - t_i^D\right)\\
&= \frac{1}{2}\int_{t_i^D}^{t_i^R}(k_x+A_x)^2dt + I_p\left(t_i^R - t_i^D\right) \doteq 0. \qquad (11)
\end{aligned}$$

Here, in the last line of Eq. (11), we have used Eq. (9) and the first equation of Eq. (10). This approximation is further confirmed by our numerical calculations, as shown in Fig. 8(a). Indeed, it is nearly zero for p_y close to the p_x axis, where the SFPH interference appears. Therefore, the first and third terms in Eq. (8) are the dominant terms accounting for the phase $\delta\theta_F$. With this in mind, Eq. (7) is simplified as

$$\delta\theta = \frac{1}{2}\int_{t_i^D}^{t_r}[p_y + A_y(t)]^2dt - \frac{1}{2}\int_{t_i^R}^{t_r}[k_y + A_y(t)]^2dt + \alpha. \qquad (12)$$

Moreover, through Eq. (9) and the first equation of Eq. (10), it can be approximated that the ionization times for

the direct electron and the rescattering electron are the same, i.e.,

$$t_i^D \doteq t_i^R. \tag{13}$$

Quantitatively, the difference in the real and imaginary parts of the ionization time are separately displayed in Figs. 8(b) and 8(c). It is indicated that for the momentum range we are interesting in, the differences are well below 0.5 a.u. Thus, this approximation is reasonable. In the following, we omit the superscript in t_i.

According to the fourth equation in Eq. (10), we have $k_y = -\frac{\int_{t_i}^{t_r} A_y(t)dt}{t_r - t_i}$. The right side of Eq. (12) can be straightforwardly simplified further,

$$\begin{aligned}
&\frac{1}{2}\int_{t_i}^{t_r}[p_y + A_y(t)]^2 dt - \frac{1}{2}\int_{t_i}^{t_r}[k_y + A_y(t)]^2 dt \\
&= \frac{1}{2}(t_r - t_i)\left(p_y^2 - k_y^2\right) + p_y\int_{t_i}^{t_r} A_y(t)dt - k_y\int_{t_i}^{t_r} A_y(t)dt \\
&= \frac{1}{2}(t_r - t_i)\left(p_y^2 - k_y^2\right) + \frac{1}{2}(t_r - t_i)\left(2k_y^2 - 2p_y k_y\right) \\
&= \frac{1}{2}(p_y - k_y)^2(t_r - t_i).
\end{aligned} \tag{14}$$

Thus we have

$$\delta\theta^{\mathrm{OTC}} = \frac{1}{2}(p_y - k_y)^2(t_r - t_i) + \alpha. \tag{15}$$

For the single-color field, $k_y = 0$, and thus the phase difference in the single-color field is written as

$$\delta\theta^{SC} = \frac{1}{2}p_y^2(t_r - t_i) + \alpha. \tag{16}$$

From Eqs. (15) and (16), we can predict the traverse momentum p_y of the SFPH interference minima and maxima in the single-color field and the OTC field. Here we take the first-order minimum of the interference fringes as an example. It is located at the position p_y where $\delta\theta = \pi$, and we obtain

$$p_y^{SC} = \sqrt{\frac{2(\pi - \alpha^{SC})}{t_r - t_i}} \tag{17}$$

and

$$p_y^{OTC} = \sqrt{\frac{2(\pi - \alpha^{OTC})}{t_r - t_i}} + k_y, \tag{18}$$

where α^{SC} and α^{OTC} are the phase due to the Coulomb interaction in the single-color field and the OTC field, respectively. Obviously, the position of the interference minimum depends on the phase of the scattering amplitude α^{SC} and α^{OTC}.

When the orthogonal second harmonic of the OTC field is a weak perturbation, $\alpha^{SC} \doteq \alpha^{OTC}$. Then the shift of the interference fringes in the OTC field with respect to that of the single-color field is written as

$$\Delta p_y = p_y^{OTC} - p_y^{SC} = \mathrm{Re}[k_y]. \tag{19}$$

It is shown that the shift of the SFPH fringes induced by the OTC field equals to k_y ($k_y = -\frac{\int_{t_i}^{t_r} A_y(t)dt}{t_r - t_i}$), and it depends on the relative phase, and also on the parallel momentum through the ionization time t_i and the rescattering time t_r. The Coulomb interaction between the parent ion and the rescattering electron influences the position of the interference fringes but does not affect the shift of the interference fringes. This is a key point of our scheme.

At last we check the validity of the approximations in Eqs. (11) and (13). In Fig. 8(d), we display the obtained Δp_y of the first minimum of the SFPH pattern as a function of relative phase φ at $p_x = -0.9$ a.u. The solid curve indicates the data calculated by Eq. (19) and the open circles are the data from Eq. (8). In Fig. 8(e), we show Δp_y for another cut at $p_x = -1.3$ a.u. The good agreement between the results of Eqs. (19) and (8) indicates the validity of our approximations. Then, with Eq. (19), we calculate Δp_y as a function of φ for p_x ranging from –1.95 to –0.75 a.u., as shown in Fig. 8(f). It is observed that the result is in good agreement with the TDSE result presented in Fig. 4(a), confirming the validation of the approximation made in Eq. (19).

D. Retrieving the complex ionization time and rescattering time

The periodic oscillation of Δp_y in Fig. 4(a) introduces us to fit its φ dependence by the function

$$\Delta p_y = P_m \cos(\varphi - \Phi_m), \tag{20}$$

where P_m describes the amplitude of the oscillation and Φ_m characterizes the relative phase where Δp_y maximizes. Figures 9(a) and 9(b) display the obtained P_m and Φ_m as functions of p_x, respectively.

P_m and Φ_m provide us two independent quantities to retrieve the complex ionization time and rescattering time. According to Eq. (19), we have

$$\begin{aligned}
\frac{\partial \Delta p_y}{\partial \varphi}|_{\varphi=\Phi_m} &= \mathrm{Re}\left[\frac{\partial k_y(t_i, t_r; \varphi)}{\partial \varphi}\right]|_{\varphi=\Phi_m} = 0, \\
\Delta p_y|_{\varphi=\Phi_m} &= \mathrm{Re}[k_y(t_i, t_r; \varphi)]|_{\varphi=\Phi_m} = P_m.
\end{aligned} \tag{21}$$

Note that t_i and t_r are complex numbers. For rescattering time t_r, it has been reported that the imaginary part is negligibly small [39,99] and thus it is a good approximation that t_r is real. So there are three quantities to be retrieved. One more independent observation is needed.

The third observation can be obtained from the relative yield ΔY, as shown in Fig. 5(a). In the OTC field, ΔY is modulated by relative phase, and it peaks at $p_y = 0$ when φ satisfies [96,97]

$$\mathrm{Re}[A_y(t_i; \varphi)]|_{\varphi=\theta_m} = 0. \tag{22}$$

This reveals that by measuring the value of the phase θ_m for maximal ΔY, we could get another observation and equation for our retrieval. In Fig. 9(c), we present θ_m extracted from the TDSE results in Fig. 5(a) as a function of p_x. This provides the third observation θ_m for determining t_i and t_r.

Before retrieving t_i and t_r, we first compare these three observations from TDSE results with those predicted by the classical model [5], QO model, and QO model with artificially setting the imaginary part in the ionization time $\mathrm{Im}[t_i] = 0$. For the quantity P_m [Fig. 9(a)], the QO model result agrees well with the TDSE result and P_m minimizes at $p_x = -1.32$ a.u., while for the classical model, the result deviates from the TDSE result obviously and the minimum of

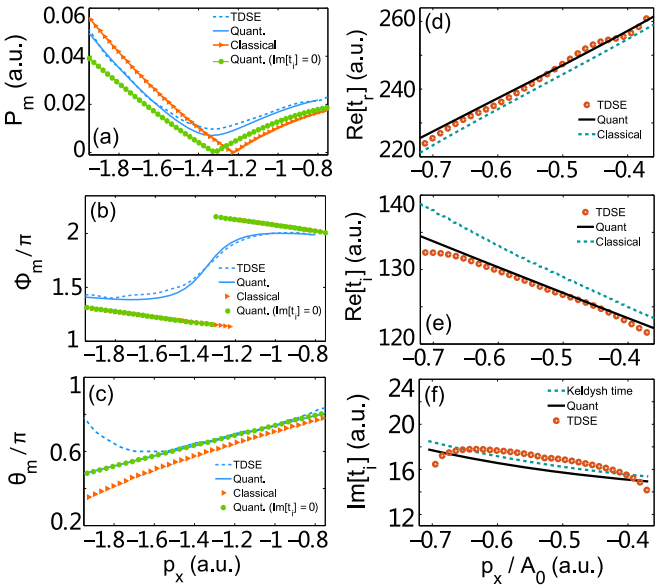

FIG. 9. (a) The amplitudes P_m extracted from the TDSE result (dashed blue curve) and predicted by the QO model (solid blue curve), classical model (red triangles), and QO model with $\mathrm{Im}[t_i] = 0$ (green dots) as functions of p_x. (b) The same as (a) but for the phase Φ_m at which Δp_y maximizes. (c) The same as (a) but for the phase θ_m where the yield ΔY peaks. (d) The real parts of the ionization times ($\mathrm{Re}[t_i]$) retrieved from the TDSE results (dots) and predicted by the QO model (solid curve) and classical model (dashed curve) as functions of p_x (scaled by the amplitude of the vector potential of the FM field A_0). (e) The same as (d) but for the rescattering times. (f) The retrieved tunneling time ($\mathrm{Im}[t_i]$). The dots show the data from the TDSE results. The solid curve represents the QO model result. The dashed curve indicates the Keldysh time.

P_m shifts towards the right. For the QO model with $\mathrm{Im}[t_i] = 0$, the prediction of P_m is smaller than the TDSE result, though the position of the minimal P_m is in coincidence with the TDSE result. For θ_m [Fig. 9(c)], the classical model result also deviates from the TDSE result, while both predictions from the QO model and QO model with $\mathrm{Im}[t_i] = 0$ agree with the TDSE result excellently for p_x not close to the boundary. This indicates that the imaginary part of t_i does not affect θ_m. For φ_m [Fig. 9(b)], the differences between the predictions of the different models and the TDSE result are much more obvious. For example, only the prediction from the QO model is in agreement with the TDSE result, and the result of the QO model with $\mathrm{Im}[t_i] = 0$ deviates seriously from the TDSE result. This indicates that the observation φ_m sensitively depends on the imaginary part of the ionization time.

With Eqs. (21) and (22), we retrieve the ionization time, including both the real and imaginary parts, and the associated rescattering time. The obtained results are shown in Figs. 9(d)– 9(f). It is indicated that both the ionization and rescattering times agree well with the predictions of the QO model and deviate distinctly from the classical model results. It is worth noting that in the classical model the ionization time is real. In the QO model, the ionization time is complex and the imaginary part is interpreted as the time for the electron tunneling through the potential barrier. With our scheme, the retrieved imaginary ionization time agrees excellently with the prediction of the QO model, as shown in Fig. 9(f). We also show the Keldysh time which is calculated by $\sqrt{2I_p}/|\vec{E}_x(t_i)|$. This imaginary time decreases as p_x moves towards zero. This is easy to understand. For p_x more close to zero, the instantaneous electric field at tunneling increases, and thus the width and height of the potential barrier decrease, leading to the decreasing of the tunneling time. We should mention that in previous studies of retrieving the ionization and rescattering times with harmonic spectroscopy, a zero or Keldysh time for the imaginary ionization time was assumed [38,57]. In our scheme, no such assumption is made. Both the real and imaginary parts of the ionization time and the rescattering time are treated as unknown quantities.

Summarizing, we have shown in detail how to retrieve the ionization and rescattering times of the electron in tunneling ionization with our attosecond photoelectron interferometer. This is based on the approximations made in Eqs. (11) and (13), the validity of which has been carefully checked. The important merit of our method is that the Coulomb interaction does not influence the shift of the SFPH fringes and thus it can be canceled. In the following sections, we confirm this point by applying our method for the model atoms with Coulomb and short potentials. We also apply our method to different targets and different parameters of the laser field.

E. Results of short-range potential

In Sec. III C, we demonstrate that the Coulomb potential does not affect the shift of the SFPH fringes and it can

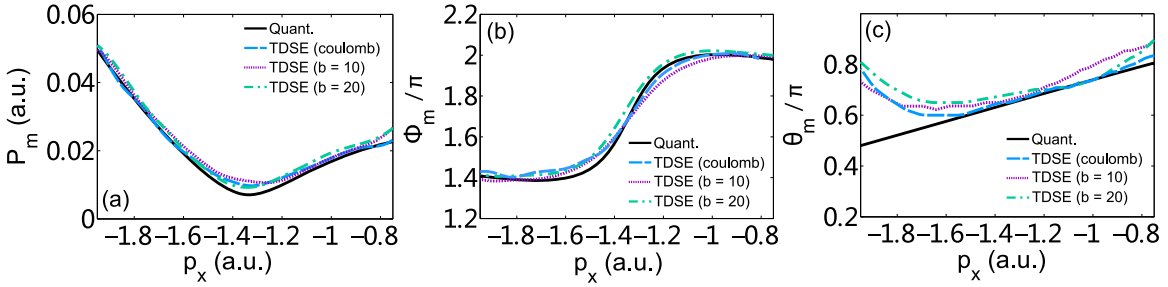

FIG. 10. (a) The amplitudes P_m extracted from the QO model results (solid black curve), and the TDSE results for the model atoms with short-range potentials $b = 10$ (dotted purple curve) and $b = 20$ (dash-dotted green curve), and the Coulomb potential (dashed blue curve). (b) The same as (a) but for the phase Φ_m. (c) The same as (a) but for the quantity θ_m.

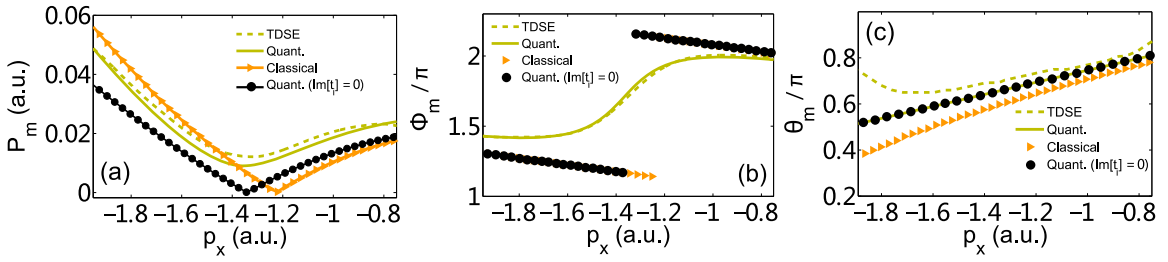

FIG. 11. The same as Figs. 7(a)– 7(c) but for Ar atom.

be safely canceled. Here, we further confirm this issue by illustrating our results for the short-range potential:

$$V(r) = -\frac{1}{\sqrt{x^2+y^2+a}} e^{-\frac{x^2+y^2}{b^2}}, \tag{23}$$

where b denotes the screening parameter. The results are illustrated by considering two values, $b = 10$ and 20. The soft-core parameter a is modulated to match the ground state of the Xe atom ($I_p = 0.446$ a.u.). Figures 10(a)– 10(c) separately show the quantities P_m, Φ_m, and θ_m extracted from the TDSE results as functions of parallel momentum p_x. For comparison, we also present the obtained TDSE results for Xe with Coulomb potential ($b = \infty$) and the QO model. Clearly, the results of the short-range potentials and Coulomb potential nicely agree with the predictions of the QO model. This confirms that the Coulomb potential does not affect the shift of the SFPH fringes.

F. Results of argon

We apply our interferometer to different atomic systems. In the QO model, the ionization and rescattering times are obtained with saddle-point method. The saddle-point equations for the direct and rescattering electrons in Eqs. (9) and (10) indicate that t_i and t_r are related to the target species through ionization energy I_p. In this section we take the Ar atom as an example.

Figure 11 shows the obtained P_m, Φ_m, and θ_m from the attosecond photoelectron interferometer. The data of the dashed curves are obtained by the TDSE calculations, and the data of the solid curves, orange triangles, and black dots are predicted by the QO model, classical model, and QO model with $\mathrm{Im}[t_i] = 0$, respectively. It is shown that P_m and Φ_m from the QO model agree excellently with the TDSE results, while those from the classical model and QO model with $\mathrm{Im}[t_i] = 0$ deviate seriously from the TDSE results. For θ_m, the classical model result shift down compared with the TDSE result, particularly at large p_x. Both the results of the QO model and QO model with $\mathrm{Im}[t_i] = 0$ are in coincidence with the TDSE result. These behaviors are the same as those of the Xe atom, as shown in Figs. 9(a)– 9(c). This confirms the effectiveness of our scheme.

G. Dependence on the frequency of the orthogonal perturbation

In the attosecond photoelectron interferometer shown above, we use the second harmonic to disturb the paths of the direct and rescattering electrons. The perturbation could be chosen as the other frequencies and our interferometer also works. Here, we take the fourth harmonic as an example. The other laser parameters are the same as those in Sec. III A.

The obtained P_m, Φ_m, and θ_m are displayed in Fig. 12, where the data of the dashed curves are extracted from the TDSE results. The green triangles, solid curves, and blue dots are the results predicted by the classical model, QO model, and the QO model with $\mathrm{Im}[t_i] = 0$, respectively. It is obvious that for the quantities P_m and Φ_m, only the results of the QO model agree well with the TDSE results, and the other models deviate from the TDSE results distinctly. For θ_m, the TDSE result is well reproduced by both the QO model and the QO model with $\mathrm{Im}[t_i] = 0$, while it is inconsistent with the classical model result. According to Eq. (19), the shift of the interference fringes is written as

$$\begin{aligned}\Delta p_y &= \mathrm{Re}[k_y] \\ &= -\mathrm{Re}\left\{\frac{E_y[\cos(q\omega t_r + \varphi) - \cos(q\omega t_i + \varphi)]}{q^2\omega^2(t_r - t_i)}\right\},\end{aligned} \tag{24}$$

where q is the harmonic order. It shows that P_m minimizes when $q\omega t_r - q\omega t_i = 2n\pi$ ($n = 1, 2, 3\ldots$), i.e., the traveling time $\Delta t = t_r - t_i = \frac{n}{q}T_0$ (T_0 is the period of the FM field). Thus for the second-harmonic perturbation ($q = 2$), there is one minimum in P_m for $p_x < 0$ [100]. For the fourth-harmonic

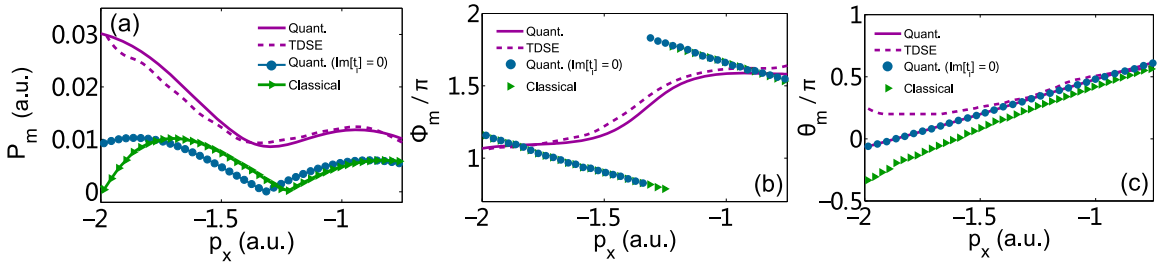

FIG. 12. The same as Figs. 7(a)– 7(c), but the orthogonal perturbation is a fourth harmonic.

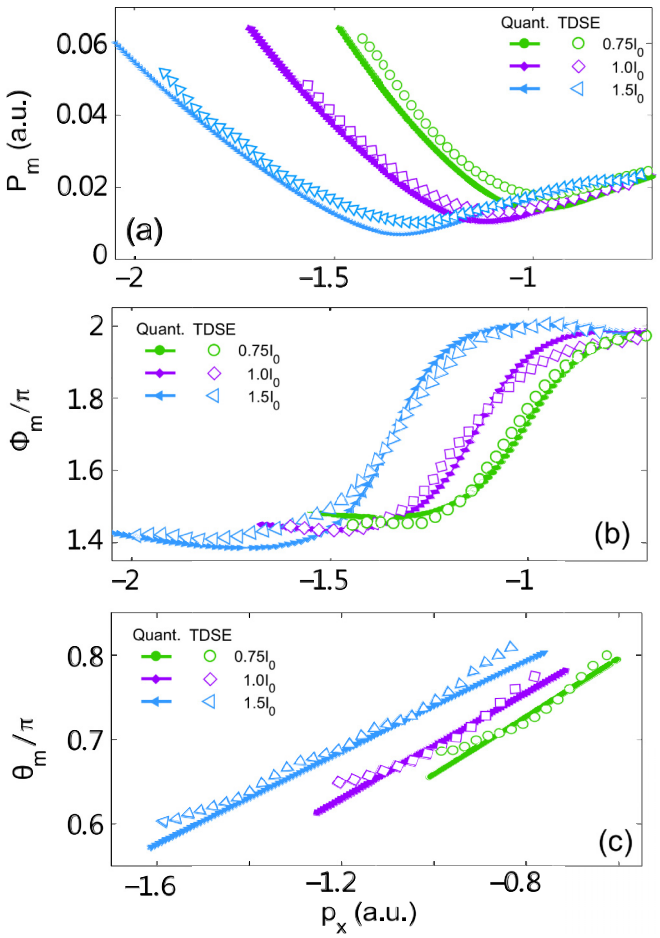

FIG. 13. (a) The amplitudes P_m as functions of p_x for the laser intensity of the FM field $I = 0.75I_0$ (green circles), $1.0I_0$ (purple diamonds), and $1.5I_0$ (blue triangles), where $I_0 = 1.0 \times 10^{14}$ W/cm^2. The open symbols represent the TDSE results and the solid symbols indicate the QO model results. (b, c). The same as (a) but for Φ_m and θ_m, respectively.

perturbation ($q = 4$), P_m minimizes at p_x where the corresponding traveling time is the 1/4, 2/4, or 3/4 cycle of the FM field. Specifically, for our laser intensity, these minima locate at $p_x = -2.20$ a.u., –1.32 a.u., and –0.40 a.u., respectively. In Fig. 12, we only show the data in the range of $p_x = -1.95$ to -0.75 a.u., and thus only one minimum is seen. Note that the minima of P_m of TDSE results and QO model results are actually not zero. This is due to the fact that the ionization time is a complex number.

H. Dependence on the intensity of the fundamental driving field

In Fig. 13, we present three observables of P_m, Φ_m, and θ_m obtained from the TDSE calculations as functions of p_x at various FM laser intensities $I = 0.75I_0$, I_0, and $1.5I_0$ ($I_0 = 1.0 \times 10^{14}$ W/cm^2), while the intensity of the orthogonal second harmonic stays unchanged (1.0×10^{12} W/cm^2). It is shown that at all intensities, these observables predicted by the QO model and extracted from the TDSE results agree well with each other. From our previous paper, we know that the quantity P_m exhibits a minimum at $p_x = 0.6A_0$ (A_0 is the amplitude of the vector potential of the FM driving field), where the traveling time is $0.5T_0$ [100]. We demonstrated that with this character the laser intensity can be accurately calibrated. For the laser intensities here, the minima locate at $p_x = -0.95$ a.u., -1.10 a.u., and -1.32 a.u., respectively, exactly corresponding to $0.6A_0$ of the FM driving fields.

IV. SUMMARY

In conclusion, we have used attosecond photoelectron interferometry, which is analogous to the optical Michelson interferometer, to resolve the temporal properties of the electron tuning ionization. In this work, we numerically investigate the PEMDs of an Xe atom for the OTC field consisting of a strong 1600-nm FM field and a perturbative second harmonic, from which we extract the SFPH pattern. Our results show that the position of the SFPH pattern is sensitive to the relative phase of the OTC field, and it shifts along the direction of the transverse momentum depending on the parallel momentum. With QO model, we reveal its origin. Moreover, we show in detail that by analyzing this shift of the SFPH pattern, the ionization time, including both the real part and imaginary part, and the related rescattering time can be retrieved accurately.

The Coulomb effect is a tough problem in intense laser-atom and/or molecule interactions and it complicates the information retrieval from the PEMDs. Here we demonstrate that it does not affect our scheme and can be safely canceled. This point is further confirmed by performing interferometry for both model atoms with the Coulomb potential and short-range potential. Additionally, we demonstrate the validity and accuracy of our scheme by applying it to the Ar atomic system, the OTC field combined by a strong FM field, and a weak fourth harmonic and different intensities of the FM field. Our work provides a reliable and versatile way to measure the time information of strong-field tunneling ionization.

ACKNOWLEDGMENTS

This work was supported by National Natural Science Foundation of China (Grants No. 11874163, No. 11622431, No. 61475055, No. 11604108, and No. 11627809) and Program for HUST Academic Frontier Youth Team.

[1] W. Becker, F. Grasbon, R. Kopold, D. B. Milošević, G. G. Paulus, and H. Walther, Above-threshold ionization: From classical features to quantum effect, Adv. At. Mol. Opt. Phys. **48**, 35 (2002).

[2] F. Krausz and M. Ivanov, Attosecond physics, Rev. Mod. Phys. **81**, 163 (2009).

[3] W. Becker, X. J. Liu, P. J. Ho, and J. H. Eberly, Theories of photoelectron correlation in laser-driven multiple atomic ionization, Rev. Mod. Phys. **84**, 1011 (2012).

[4] L. Peng, W. Jiang, J. Geng, W. Xiong, and Q. Gong, Tracing and controlling electronic dynamics in atoms and molecules by attosecond pulses, Phys. Rep. **575**, 1 (2015).

[5] P. B. Corkum, Plasma Perspective on Strong Field Multiphoton Ionization, Phys. Rev. Lett. **71**, 1994 (1993).
[6] G. G. Paulus, W. Nicklich, H. Xu, P. Lambropoulos, and H. Walther, Plateau in Above Threshold Ionization Spectra, Phys. Rev. Lett. **72**, 2851 (1994).
[7] P. Salières, B. Carré, L. L. Déroff, F. Grasbon, G. G. Paulus, H. Walther, R. Kopold, W. Becker, D. B. Milošević, A. Sanpera, and M. Lewenstein, Feynman's path-integral approach for intense-laser-atom interactions, Science **292**, 902 (2001).
[8] H. Kang, W. Quan, Y. Wang, Z. Lin, M. Wu, H. Liu, X. Liu, B. B. Wang, H. J. Liu, Y. Q. Gu, X. Y. Jia, J. Liu, J. Chen, and Y. Cheng, Structure Effect in Angle-Resolved High-Order Above-Threshold Ionization of Molecules, Phys. Rev. Lett. **104**, 203001 (2010).
[9] B. Walker, B. Sheehy, L. F. DiMauro, P. Agostini, K. J. Schafer, and K. C. Kulander, Precision Measurement of Strong Field Double Ionization of Helium, Phys. Rev. Lett. **73**, 1227 (1994).
[10] X. Ma, Y. Zhou, Y. Chen, M. Li, Y. Li, Q. Zhang, and P. Lu, Timing the release of the correlated electrons in strong-field nonsequential double ionization by circularly polarized two-color laser fields, Opt. Express **27**, 1825 (2019).
[11] Y. Zhou, Q. Liao, and P. Lu, Asymmetric electron energy sharing in strong-field double ionization of helium, Phys. Rev. A **82**, 053402 (2010).
[12] Y. Zhou, C. Huang, and P. Lu, Coulomb-tail effect of electron-electron interaction on nonsequential double ionizaiton, Phys. Rev. A **84**, 023405 (2011).
[13] Y. Zhou, C. Huang, A. Tong, Q. Liao, and P. Lu, Correlated electron dynamics in nonsequential double ionization by orthogonal two-color laser pulses, Opt. Express **19**, 2301 (2011).
[14] Y. Zhou, C. Huang, Q. Liao, and P. Lu, Classical Simulations Including Electron Correlations for Sequential Double Ionization, Phys. Rev. Lett. **109**, 053004 (2012).
[15] X. Ma, Y. Zhou, N. Li, M. Li, and P. Lu, Attosecond control of correlated electron dynamics in strong-field nonsequential double ionization by parallel two-color pulses, Opt. Laser. Technol. **108**, 235 (2018).
[16] M. Ferray, A. L'Huillier, X. F. Li, L. A. Lompré, G. Mainfray, and C. Manus, Multiple-harmonic conversion of 1064 nm radiation in rare gases, J. Phys. B **21**, L31 (1988).
[17] J. L. Krause, K. J. Schafer, and K. C. Kulander, High-Order Harmonic Generation from Atoms and Ions in the High Intensity Regime, Phys. Rev. Lett. **68**, 3535 (1992).
[18] E. Constant, D. Garzella, P. Breger, E. Mével, C. Dorrer, C. Le Blanc, F. Salin, and P. Agostini, Optimizing High Harmonic Generation in Absorbing Gases: Model and Experiment, Phys. Rev. Lett. **82**, 1668 (1999).
[19] L. He, P. Lan, A T. Le, B. Wang, B. Wang, X. Zhu, P. Lu, and C. D. Lin, Real-Time Observation of Molecular Spinning with Angular High-Harmonic Spectroscopy, Phys. Rev. Lett. **121**, 163201 (2018).
[20] X. Zhang, X. Zhu, D. Wang, L. Li, X. Liu, Q. Liao, P. Lan, and P. Lu, Ultrafast oscillating-magnetic-field generation based on electronic-current dynamics, Phys. Rev. A **99**, 013414 (2019).
[21] G. Sansone, E. Benedetti, F. Calegari, C. Vozzi, L. Avaldi, R. Flammini, L. Poletto, P. Villoresi, C. Altucci, R. Velotta, S. Stagira, S. D. Silvestri, and M. Nisoli, Isolated single-cycle attosecond pulses, Science **314**, 443 (2006).
[22] E. Goulielmakis, M. Schultze, M. Hofstetter, V. S. Yakovlev, J. Gagnon, M. Uiberacker, A. L. Aquila, E. M. Gullikson, D. T. Attwood, R. Kienberger, F. Krausz, and U. Kleineberg, Single-cycle nonlinear optics, Science **320**, 1614 (2008).
[23] T. Gaumnitz, A. Jain, Y. Pertot, M. Huppert, I. Jordan, F. A. Lamas, and H. J. Wörner, Streaking of 43-attosecond soft-X-ray pulses generated by a passively CEP-stable mid-infrared driver, Opt. Express **25**, 27506 (2017).
[24] J. Li, X. Ren, Y. Yin, K. Zhao, A. Chew, Y. Cheng, E. Cunningham, Y. Wang, S. Hu, Y. Wu, M. Chini, and Z. Chang, 53-attosecond X-ray pulses reach the carbon K-edge, Nat. Commun. **8**, 186 (2017).
[25] J. Itatani, J. Levesque, D. Zeidler, H. Niikura, H. Pépin, J. C. Kieffer, P. B. Corkum, and D. M. Villeneuve, Tomographic imaging of molecular orbitals, Nature (London) **432**, 867 (2004).
[26] H. Yuan, L. He, F. Wang, B. Wang, X. Zhu, P. Lan, and P. Lu, Tomography of asymmetric molecular orbits with a one-color inhomogeneous field, Opt. Lett. **43**, 931 (2018).
[27] T. Zuo, A. D. Bandrauk, P. B. Corkum, Laser-induced electron diffraction: A new tool for probing ultrafast, molecular dynamics. Chem. Phys. Lett. **259**, 313 (1996).
[28] T. Morishita, A-T. Le, Z. Chen, and C. D. Lin, Accurate Retrieval of Structural Information from Laser-Induced Photoelectron and High-Order Harmonic Spectra by Few-Cycle Laser Pulses, Phys. Rev. Lett. **100**, 013903 (2008).
[29] C. I. Blaga, J. Xu, A. D. DiChiara, E. Sistrunk, K. Zhang, P. Agostini, T. A. Miller, L. F. DiMauro, and C. D. Lin, Imaging ultrafast molecular dynamics with laser-induced electron diffraction, Nature (London) **483**, 194 (2012).
[30] B. Wolter, M. G. Pullen, A-T. Le, M. Baudisch, K. D. Dier, A. Senftleben, M. Hemmer, C. D. Schröter, J. Ullrich, T. Pfeifer, R. Moshammer, S. Gräfe, O. Vendrell, C. D. Lin, and J. Biegert, Ultrafast electron diffraction imaging of bond breaking in di-ionized acetylene, Science **354**, 308 (2016).
[31] E. H. Hauge and J. A. Støavneng, Tunneling times: A critical review, Rev. Mod. Phys. **61**, 917 (1989).
[32] P. Eckle, A. N. Pfeiffer, C. Cirelli, A. Staudte, R. Dörner, H. G. Muller, M. Büttiker, and U. Keller, Attosecond ionization and tunneling delay time measurements in helium, Science **322**, 1525 (2008).
[33] A. N. Pfeiffer, C. Cirelli, M. Smolarski, D. Dimitrovski, M. Abu-samha, L. B. Madsen, and U. Keller, Attoclock reveals natural coordinates of the laser-induced tunneling current flow in atoms, Nat. Phys. **8**, 76 (2012).
[34] L. Torlina, F. Morales, J. Kaushal, I. Ivanov, A. Kheifets, A. Zielinski, A. Scrinzi, H. G. Muller, S. Sukiasyan, M. Ivanov, and O. Smirnova, Interpreting attoclock measurements of tunneling times, Nat. Phys. **11**, 503 (2015).
[35] N. Camus, E. Yakaboylu, L. Fechner, M. Klaiber, M. Laux, Y. Mi, K. Z. Hatsagortsyan, T. Pfeifer, C. H. Keitel, and R. Moshammer, Experimental Evidence for Quantum Tunneling Time, Phys. Rev. Lett. **119**, 023201 (2017).
[36] R. Wang, Q. Zhang, D. Li, S. Xu, P. Cao, Y. Zhou, W. Cao, and P. Lu, Identification of tunneling and multiphoton ionization in intermediate Keldysh parameter regime, Opt. Express **27**, 6471 (2019).
[37] M. Lein, Atomic physics: Electrons get real, Nature (London) **485**, 313 (2012).

[38] D. Shafir, H. Soifer, B. D. Bruner, M. Dagan, Y. Mairesse, S. Patchkovskii, M. Y. Ivanov, O. Smirnova, and N. Dudovich, Resolving the time when an electron exits a tunneling barrier, Nature (London) **484**, 343 (2012).

[39] O. Pedatzur, G. Orenstein, V. Serbinenko, H. Soifer, B. D. Bruner, A. J. Uzan, D. S. Brambila, A. G. Harvey, L. Torlina, F. Morales, O. Smirniva, and N. Dudovich, Attosecond tunneling interferometry, Nat. Phys. **11**, 815 (2015).

[40] M. Ivanov, M. Spanner, and O. Smirnova, Anatomy of strong field ionization, J. Mod. Opt. **52**, 165 (2005).

[41] J. M. Dahlström, A. L'Huillier, and J. Mauritsson, Quantum mechanical approach to probing the birth of attosecond pulses using a two-color field, J. Phys. B **44**, 095602 (2011).

[42] L. V. Keldysh, Ionization in the field of a strong electromagnetic wave, Sov. Phys. JETP **20**, 1307 (1965).

[43] A. M. Perelomov, V. S. Popov, and M. V. Terent'ev, Ionization of atoms in an alternating electric field: II, Sov. Phys. JETP **24**, 207 (1967).

[44] V. S. Popov, V. P. Kuznetsov, and A. M. Perelomov, Quansicalssical approximation for nonstationary problems, Sov. Phys. JETP **26**, 222 (1968).

[45] V. P. Kuznetsov, A. M. Perelomov, and V. S. Popov, Quansicalssical approximation in ionization problems, Sov. Phys. JETP **27**, 616 (1968).

[46] S. Baker, J. S. Robinson, C. A. Haworth, H. Teng. R. A. Smith, C. C. Chirilă, M. Lein, J. W. G. Tisch, and J. P. Marangos, Probing proton dynamics in molecules on an attosecond time scale, Science **312**, 424 (2006).

[47] W. Li, X. Zhou, R. Lock, S. Patchkovskii, A. Stolow, H. Kapteyn, and M. Murnane, Time-resolved dynamics in N_2O_4 probed using high harmonic generation, Science **322**, 1207 (2008).

[48] O. Smirnova, Y. Mairesse. S. Patchkovskii, N. Dudovich, D. Villeneuve, P. Corkum, and M. Y. Ivanov, High harmonic interferometry of multi-electron dynamics in molecules, Nature (London) **460**, 972 (2009).

[49] X. Xie, S. Roither, D. Kartashov, E. Persson, D. G. Arbó, L. Zhang, S. Gräfe, M. S. Schöffler, J. Burgdörfer, Andrius Baltuška, and M. Kitzler, Attosecond Probe of Valence-Electron Wave Packets by Subcycle Sculpted Laser Fields, Phys. Rev. Lett. **108**, 193004 (2012).

[50] P. Kraus, B. Mignolet, D. Baykusheva, A. Rupenyan, L. Horný, E. Penka, G. Grassi, O. Tolstikhin, J. Schneider, F. Jensen, L. Madsen, A. Bandrauk, F. Remacle, and H. Wörner, Measurement and laser control of attosecond charge migration in ionized iodoacetylene, Science **350**, 790 (2015).

[51] M. Haertelt, X.-B. Bian, M. Spanner, A. Staudte, and P. B. Corkum, Probing Molecular Dynamics by Laser-Induced Backscattering Holography, Phys. Rev. Lett. **116**, 133001 (2016).

[52] G. L. Yudin and M. Y. Ivanov, Nonadiabatic tunnel ionization: Looking inside a laser cycle, Phys. Rev. A **64**, 013409 (2001).

[53] V. D. Mur, S. V. Popruzhenko, and V. S. Popov, Energy and momentum spectra of photoelectrons under conditions of ionization by strong laser radiation (the case of elliptic polarization), J. Exp. Theor. Phys. **92**, 777 (2001).

[54] I. Barth and O. Smirnova, Nonadiabatic tunneling in circularly polarized laser fields, II. Derivation of formulas, Phys. Rev. A **87**, 013433 (2013).

[55] M. Li, J.-W. Geng, M. Han, M.-M. Liu, L.-Y. Peng, Q. Gong, and Y. Liu, Subcycle nonadiabatic strong-field tunneling ionization, Phys. Rev. A **93**, 013402 (2016).

[56] K. Liu, S. Luo, M. Li, Y. Li, Y. Feng, B. Du, Y. Zhou, P. Lu, and I. Barth, Detecting and Characterizing the Nonadiabaticity of Laser-Induced Quantum Tunneling, Phys. Rev. Lett. **122**, 053202 (2019).

[57] J. Zhao and M. Lein, Determination of Ionization and Tunneling Times in High-Order Harmonic Generation, Phys. Rev. Lett. **111**, 043901 (2013).

[58] Y. Huismans, A. Rouzée, A. Gijsbertsen, J. Jungmann, A. Smolkowska, P. Logman, F. Lépine, C. Cauchy, S. Zamith, T. Marchenko, J. Bakker, G. Berden, B. Redlich, A. van der Meer, H. Muller, W. Vermin, K. Schafer, M. Spanner, M. Ivanov, O. Smirnova, D. Bauer, S. Popruzhenko, and M. Vrakking, Time-resolved holography with photoelectrons, Science **331**, 61 (2011).

[59] D. D. Hickstein, P. Ranitovic, S. Witte, X.-M. Tong, Y. Huismans, P. Arpin, X. Zhou, K. E. Keister, C. W. Hogle, B. Zhang, C. Ding, P. Johnsson, N. Toshima, M. J. J. Vrakking, M. M. Murnane, and H. C. Kapteyn, Direct Visualization of Laser-Driven Electron Multiple Scattering and Tunneling Distance in Strong-Field Ionization, Phys. Rev. Lett. **109**, 073004 (2012).

[60] D. G. Arbó, C. Lemell, S. Nagele, N. Camus, L. Fechner, A. Krupp, T. Pfeifer, S. D. López, R. Moshammer, and J. Burgdörfer, Ionization of argon by two-color laser pulses with coherent phase control, Phys. Rev. A **92**, 023402 (2015).

[61] L. Fechner, N. Camus, A. Krupp, J. Ullrich, T. Pfeifer, and R. Moshammer, Creation and survival of autoionizing states in strong laser fields, Phys. Rev. A **92**, 051403 (2015).

[62] H. Xie, M. Li, S. Luo, Y. Li, J. Tan, Y. Zhou, W. Cao, and P. Lu, Photoelectron holography and forward scattering in atomic ionization by elliptically polarized laser pulses, Opt. Lett. **43**, 3220 (2018).

[63] M. Meckel, A. Staudte, S. Patchkovskii, D. M. Villeneuve, P. B. Corkum, R. Dörner, and M. Spanner, Signatures of the continuum electron phase in molecular strong-field photoelectron holography, Nat. Phys. **10**, 594 (2014).

[64] S. G. Walt, N. B. Ram, M. Atala, N. I. S. Shilovski, A. Conta, D. Baykusheva, M. Lein, and H. J. Wörner, Dynamics of valence-shell electrons and nuclei probed by strong-field holography and rescattering, Nat. Commun. **8**, 15651 (2017).

[65] Y. Huismans, A. Gijsbertsen, A. S. Smolkowska, J. H. Jungmann, A. Rouzée, P. S. W. M. Logman, F. Lépine, C. Cauchy, S. Zamith, T. Marchenko, J. M. Bakker, G. Berden, B. Redlich, A. F. G. van der Meer. Ivanov, M. Yu, T.-M. Yan, D. Bauer, O. Smirnova, and M. J. J. Vrakking, Scaling Laws for Photoelectron Holography in the Midinfrared Wavelength Regime, Phys. Rev. Lett. **109**, 013002 (2012).

[66] X.-B. Bian and A. D. Bandrauk, Attosecond Time-Resolved Imaging of Molecular Structure by Photoelectron Holography, Phys. Rev. Lett. **108**, 263003 (2012).

[67] M. He, Y. Li, Y. Zhou, M. Li, and P. Lu, Temporal and spatial manipulation of the recolliding wave packet in strong-field photoelectron holography, Phys. Rev. A **93**, 033406 (2016).

[68] W. Yang, H. Zhang, C. Lin, J. Xu, Z. Sheng, X. Song, S. Hu, and J. Chen, Momentum mapping of continuum-electron wave-packet interference, Phys. Rev. A **94**, 043419 (2016).

[69] M. M. Liu, M. Li, C. Wu, Q. Gong, A. Staudte, and Y. Liu, Phase Structure of Strong-Field Tunneling Wave Packet from Molecules, Phys. Rev. Lett. **116**, 163004 (2016).

[70] Y. Li, Y. Zhou, M. He, M. Li, and P. Lu, Identifying backward-rescattering photoelectron hologram with orthogonal two-color laser fields, Opt. Express **24**, 23697 (2016).

[71] Y. Zhou, O. I. Tolstikhin, and T. Morishita, Near-Forward Rescattering Photoelectron Holography in Strong-Field Ionization: Extraction of the Phase of the Scattering Amplitude, Phys. Rev. Lett. **116**, 173001 (2016).

[72] M. He, Y. Zhou, Y. Li, M. Li, and P. Lu, Revealing the target structure information encoded in strong-field photoelectron hologram, Opt. Quant. Electron. **49**, 232 (2017).

[73] M. Li, W.-C Jiang, H. Xie, S. Luo, Y. Zhou, and P. Lu, Strong-field photoelectron holography of atoms by bicircular two-color laser pulses, Phys. Rev. A **97**, 023415 (2018).

[74] Q. Xia, J. Tao, J. Cai L. Fu, and J. Liu, Quantum Interference of Glory Rescattering in Strong-Field Atomic Ionization, Phys. Rev. Lett. **121**, 143201 (2018).

[75] M. He, Y. Li, Y. Zhou, M. Li, W. Cao, and P. Lu, Direct Visualization of Valence Electron Motion Using Strong-Field Photoelectron Holography, Phys. Rev. Lett. **120**, 133204 (2018).

[76] J. Tan, Y. Zhou, M. He, Y. Chen, Q. Ke, J. Liang, X. Zhu, M. Li, and P. Lu, Determination of the Ionization Time Using Attosecond Photoelectron Interferometry, Phys. Rev. Lett. **121**, 253203 (2018).

[77] C. I. Blaga, F. Catoire, P. Colosimo, G. G. Paulus, H. G. Muller, P. Agostini, and L. F. Dimauro, Strong-field photoionization revisited, Nat. Phys. **5**, 335 (2009).

[78] W. Quan, Z. Lin, M. Wu, H. Kang, H. Liu, X. Liu, J. Chen, J. Liu, X. T. He, S. G. Chen, H. Xiong, L. Guo, H. Xu, Y. Fu, Y. Cheng, and Z. Z. Xu, Classical Aspects in Above-Threshold Ionization with a Midinfrared Strong Laser Field, Phys. Rev. Lett. **103**, 093001 (2009).

[79] C. Y. Wu, Y. D. Yang, Y. Q. Liu, Q. H. Gong, M. Y. Wu, X. Liu, X. L. Hao, W. D. Li, X. T. He, and J. Chen, Characteristic Spectrum of Very Low-Energy Photoelectron from Above-Threshold Ionization in the Tunneling Regime, Phys. Rev. Lett. **109**, 043001 (2012).

[80] Y. Qin, M. Li, Y. Li, M. He, S. Luo, Y. Liu, Y. Zhou, and P. Lu, Asymmetry of the photoelectron momentum distribution from molecular ionization in elliptically polarized laser pulses, Phys. Rev. A **99**, 013431 (2019).

[81] X. Bian and A. D. Bandrauk, Orientation-dependent forward-backward photoelectron holography from asymmetric molecules, Phys. Rev. A. **89**, 033423 (2014).

[82] W. Becker and D. B. Milošević, Above-threshold ionization for very low electron energy, J. Phys. B **48**, 151001 (2015).

[83] X. Song, J. Xu, C. Lin, Z. Sheng, P. Liu, X. Yu, H. Zhang, and W. Yang, Attosecond interference induced by Coulomb-field-driven transverse backward-scattering electron wave packets, Phys. Rev. A. **95**, 033426 (2017).

[84] M. D. Feit, J. A. Fleck, and A. Steiger, Solution of the schrödinger equation by a spectral method, J. Comput. Phys. **47**, 412 (1982).

[85] M. Protopapas, C. H. Keitel, and P. L. Knight, Atomic physics with super-high intensity lasers, Rep. Prog. Phys. **60**, 389 (1997).

[86] X. Tong, K. Hino, and N. Toshima, Phase-dependent atomic ionization in few-cycle intense laser fields, Phys. Rev. A **74**, 031405 (2006).

[87] S. Chelkowski, C. Foisy, and A. D. Bandrauk, Electron-nuclear dynamics of multiphoton H_2^+ dissociative ionization intense laser fields, Phys. Rev. A **57**, 1176 (1998).

[88] X. Tong, S. Watahiki, K. Hino, and N. Toshima, Numerical Observation of the Rescattering Wave Packet in Laser-Atom Interaction, Phys. Rev. Lett. **99**, 093001 (2007).

[89] P. He, N. Takemoto, and F. He, Photoelectron momentum distribution of atomic and molecular systems in strong circularly or elliptically polarized laser field, Phys. Rev. A **91**, 063413 (2015).

[90] D. B. Milošević, G. G. Paulus, D. Bauer, and W. Becker, Above-threshold ionization by few-cycle pulses, J. Phys. B **39**, R203 (2006).

[91] F. Lindner, M. G. Schätzel, H. Walther, A. Baltuška, E. Goulielmakis, F. Krausz, D. B. Milošević, D. Bauer, W. Becker, and G. G. Paulus, Attosecond Double-Slit Experiment, Phys. Rev. Lett. **95**, 040401 (2005).

[92] D. G. Arbó, E. Persson, and J. Burgdörfer, Time double-slit interferences in strong-field tunneling ionization, Phys. Rev. A **74**, 063407 (2006).

[93] M. Richter, M. Kunitski, M. Schöffler, T. Jahnke, L. P. H. Schmidt, M. Li, Y. Liu, and R. Dörner, Streaking Temporal Double-Slit Interference by an Orthogonal Two-Color Laser Field, Phys. Rev. Lett. **114**, 143001 (2015).

[94] T. Marchenko, Y. Huismans, K. J. Schafer, and M. J. J. Vrakking, Criteria for the observation of strong-field photoelectron holography, Phys. Rev. A **84**, 053427 (2011).

[95] H. Xie, M. Li, Y. Li, Y. Zhou, and P. Lu, Intra-half-cycle interference of low-energy photoelectron in strong midinfrared laser fields, Opt. Express **24**, 27726 (2016).

[96] J. Henkel and M. Lein, Analysis of electron trajectories with two-color strong-field ionization, Phys. Rev. A **92**, 013422 (2015).

[97] N. Eicke and M. Lein, Extracting trajectory information from two-color strong-field ionization, J. Mod. Opt. **64**, 981 (2017).

[98] G. Porat, G. Alon, S. Rozen, O. Pedatzur, M. Krüger, D. Azoury, A. Natan, G. Orenstein, B. Bruner, M. Vrakking, and N. Dudovich, Attosecond time-resolved photoelectron holography, Nat. Commun. **9**, 2805 (2018).

[99] E. V. van der Zwan and M. Lein, Molecular Imaging Using High-Order Harmonic Generation and Above-Threshold Ionization, Phys. Rev. Lett. **108**, 043004 (2012).

[100] J. Tan, Y. Zhou, M. Li, M. He, Y. Liu, and P. Lu, Accurate measurement of laser intensity using photoelectron interference in strong-field tunneling ionization, Opt. Express **26**, 20063 (2018).